Geospatial characterization of immune cell distributions and dynamics across the microenvironment in renal cell carcinoma

Nicholas Chakiryan (Nicholas.Chakiryan@moffitt.org)
Department of Genitourinary Oncology, Moffitt Cancer Center

Youngchul Kim
Department of Cancer Epidemiology, Moffitt Cancer Center

Anders Berglund
Moffitt Cancer Center https://orcid.org/0000-0002-0393-3530

Gregory Kimmel
Department of Integrated Mathematical Oncology, Moffitt Cancer Center

Andrew Chang
Moffitt Cancer Center

Ali Hajiran
Department of Genitourinary Oncology, Moffitt Cancer Center

Jonathan Nguyen
Department of Pathology, Moffitt Cancer Center https://orcid.org/0000-0001-6146-2047

Carlos Moran
H. Lee Moffitt Cancer Center

Daryoush Saeed-Vafa
Department of Pathology, Moffitt Cancer Center

Esther Katende
Department of Genitourinary Oncology, Moffitt Cancer Center,

Neale Lopez-Blanco
Department of Pathology, Moffitt Cancer Center

Jad Chahoud
Department of Genitourinary Oncology, Moffitt Cancer Center

Phillip Rappold
Urology Service, Department of Surgery, Memorial Sloan Kettering Cancer Center

Phillip Spiess
Department of Genitourinary Oncology, Moffitt Cancer Center https://orcid.org/0000-0002-5723-1972

Michelle Fournier
Department of Genitourinary Oncology, Moffitt Cancer Center

Daniel Jeong

Department of Radiology, Moffitt Cancer Center

Liang Wang

Department of Tumor Biology, Moffitt Cancer Center https://orcid.org/0000-0002-9364-8572

Dongliang Du

Department of Biostatistics and Bioinformatics, Moffitt Cancer Center

Jamie Teer

Department of Biostatistics and Bioinformatics, Moffitt Cancer Center https://orcid.org/0000-0003-4513-0282

Jasreman Dhillon

Department of Pathology, Moffitt Cancer Center

Ari Hakimi

MSKCC https://orcid.org/0000-0002-0930-8824

Phillip Altrock

Max Planck Institute for Evolutionary Biology

James Mule

H. Lee Moffitt Cancer Center

Brandon Manley

Department of Genitourinary Oncology, Moffitt Cancer Center

Article

Keywords: immune cell markers, immunofluorescence, renal cell carcinoma, clear cell renal cell carcinoma, tumor immune microenvironment, tumor associated macrophages

Posted Date: September 14th, 2021

DOI: https://doi.org/10.21203/rs.3.rs-847697/v1

Geospatial characterization of immune cell distributions and dynamics across the microenvironment in renal cell carcinoma

Nicholas H Chakiryan[1], Youngchul Kim[2], Anders Berglund[2], Andrew Chang[1], Gregory J Kimmel[3], Ali Hajiran[1], Jonathan Nguyen[4], Carlos Moran-Segura[4], Daryoush Saeed-Vafa[4], Esther Katende[1], Neale Lopez-Blanco[4], Jad Chahoud[1], Phillip Rappold[5], Philippe E Spiess[1], Michelle Fournier[1], Daniel Jeong[6], Liang Wang[7], Dongliang Du [2], Jamie K Teer[2], Jasreman Dhillon[4], A Ari Hakimi[5], Philipp M Altrock[3], James Mulé[6], and Brandon J Manley[1]

[1]Department of Genitourinary Oncology, H Lee Moffitt Cancer Center and Research Institute, Tampa, FL, USA
[2]Department of Biostatistics and Bioinformatics, H Lee Moffitt Cancer Center and Research Institute, Tampa, FL, USA
[3] Integrated Mathematical Oncology Department, H Lee Moffitt Cancer Center and Research Institute, Tampa, FL, USA
[4]Department of Pathology, H Lee Moffitt Cancer Center, Tampa, FL, USA
[5]Urology Service, Department of Surgery, Memorial Sloan Kettering Cancer Center, New York, NY, USA
[6]Department of Radiology, H Lee Moffitt Cancer Center, Tampa, FL, USA
[7]Department of Tumor Biology, H Lee Moffitt Cancer Center and Research Institute, Tampa, FL, USA
[8]Immunology Department, H Lee Moffitt Cancer Center and Research Institute, Tampa, FL, USA

Corresponding author:
Nicholas Chakiryan, MD
H. Lee Moffitt Cancer Center and Research Institute
12902 Magnolia Drive, Tampa, FL 33612
Email: Nicholas.chakiryan@moffitt.org

Keywords: immune cell markers; immunofluorescence; renal cell carcinoma; clear cell renal cell carcinoma; tumor immune microenvironment; tumor associated macrophages

Word count: 6,200

Character count: 42,160

Running title: Geospatial and genomic landscape of RCC

INTRODUCTION

Since the emergence of immune checkpoint inhibiting (ICI) systemic immunotherapy in the management of metastatic renal cell carcinoma (RCC), detailed investigations into the tumor-immune microenvironment (TIME) of RCC have become critically important[1-6]. Only a subset of patients will have an objective response to ICIs, but responses can be substantial and durable[7]. Given this response profile, identifying biomarkers for response and resistance to ICI is a vital area of research. The overarching goal of this work is to select patients for ICI therapy and identify adjunctive targetable pathways to increase the proportion of patients achieving objective and durable responses.

Tumor mutational burden (TMB), PD-L1 expression, and CD8+ T-cell infiltration have emerged as promising biomarkers predicting response to ICI-based regimens across a wide spectrum of tumor primary sites and histologies [8-10]. However, in clear cell RCC (ccRCC) these biomarkers have not performed particularly well in either a predictive or prognostic capacity [11-14]. Despite being one of the most immune-inflamed tumor types, ccRCC tumors harbor a relatively modest TMB [13]. A recent meta-analysis of ICI trials in RCC did not demonstrate improved overall survival (OS) for patients with PD-L1+ versus PD-L1- tumors, though it was predictive for progression-free survival (PFS)[15]. Additionally, CD8+ infiltration does not consistently confer improved ICI response in ccRCC, and has often been paradoxically associated with poor outcomes[16-18]. These results point to the ccRCC TIME as being uniquely complex, with clinical outcomes not being driven by the same factors that have been identified in other solid-organ malignancies[19].

Leveraging single-cell RNA-sequencing (scRNA-seq), recent investigations into the ccRCC TIME have implicated M2-like tumor-associated macrophages (TAMs) as having a pro-tumor immunosuppressive effect on the TIME of ccRCC[20-23]. Several of these studies have identified a possible interaction between M2-like TAMS and CD8+ T-cells that results in switching CD8+ T-cells into a terminally exhausted state, resulting in poor clinical outcomes[20-22]. These findings partially explain the

paradoxical association between increasing CD8+ infiltration and poor outcomes in ccRCC and demonstrate the emerging importance of recognizing distinct TAM subtypes and their biological actions in ccRCC.

However, scRNA-seq methodologies are tissue-destructive, impeding the ability to analyze the effect of immune cell geospatial location and distribution. TAMs affect the TIME through a variety of receptor-binding and paracrine mechanisms that rely on proximity to their effector cells, and the specific location and geospatial distribution of TAMs has been shown to have a significant impact on their pro-tumor activity[24-27].

Herein, we performed multiplex immunofluorescence (mIF) using an array of myeloid and lymphoid markers on primary tumor samples from 122 patients with RCC. Regions of interest (ROIs) were selected from three distinct tumor zones: the tumor-core, stroma, and tumor-stroma interface. Digital pathologic imaging analysis was leveraged to quantify the geospatial location and distribution of immune cells within the TIME, and these findings were correlated with a variety of tumor molecular profiles. For patients with ccRCC, as clinical stage increased, immunosuppressive M2-like CD163+ TAMs migrated from the tumor compartment and into the stroma at the tumor-stroma interface and became increasingly co-localized with CD8+ T-cells. Furthermore, high CD163+ TAM clustering into the stromal compartment and high CD8+/CD163+ stromal co-localization were independently associated with worse OS and cancer-specific survival (CSS), while accounting for clinical stage. Overall, this data suggests that the pro-tumor effect of M2-like TAMs and their effect on CD8+ T-cells may be dependent on their specific geospatial location and distribution within the TIME -- namely, that M2-like TAMs exert their pro-tumor effect and interact with CD8+ T-cells most effectively from the stromal compartment at the tumor-stroma interface.

RESULTS

Study Population

The overall study population included 122 patients who had surgically excised RCC samples that underwent mIF (Age: 66 years (IQR 59-72); Male gender: 85 (70%); White race: 107 (88%)). Histology was ccRCC in 97 patients (80%), papillary RCC in 17 (14%), and chromophobe RCC in 5 (4%). The cohort included patients with a wide spectrum of clinical disease states: 29 patients (24%) presenting with clinical stage I/II, 62 (51%) with clinical stage III, and 31 (25%) with clinical stage IV. **(Table 1) (Figure 1)**

RCC Histologic Subtype affects the Immune Landscape of the TIME

Quantitative digital pathologic image analysis was utilized to abstract immune cell density from each ROI, which was averaged within three sampled histologic zones (tumor-core [2 ROIs per patient], tumor-stroma interface [3 ROIs], and stroma [2 ROIs]) for each patient.

When stratified by RCC histologic subtype, significant differences in immune density were identified. Within the tumor-core zone, ccRCC samples, as compared with papillary RCC, had higher median TBET density (30 vs. 6 cells/mm2; $p < 0.001$), higher FOXP3 density (6 vs. 0 cells/mm2; $p < 0.001$), lower CD68 density (244 vs. 492 cells/mm2; $p < 0.001$), and lower CD206 density (53 vs. 163 cells/mm2; $p = 0.03$). Comparing ccRCC samples with chromophobe RCC within the tumor zone found a higher CD3 density (50 vs. 0 cells/mm2; $p = 0.01$), higher CD8 density (76 vs. 3 cells/mm2; $p = 0.01$), higher FOXP3 density (6 vs. 0 cells/mm2; $p = 0.04$), and higher CD20 density (2 vs. 0 cells/mm2; $p = 0.03$) (**Figure 2A**).

Additional comparisons for the tumor-stroma interface and stromal zones can be found in **Figures 2B and 2C**. Examples of ccRCC, papillary RCC, and chromophobe RCC mIF samples, using our lymphoid panel, can be found in **Figures 2D-F**.

The remainder of the presented analyses focus exclusively on patients with ccRCC histology.

ccRCC Immune Cell Density is Most Often Highest at the Tumor-stroma Interface

When stratified by tumor zone and cell type, the tumor-stroma interface most often contained the highest cellular density. CD3, CD8, FOXP3, T-bet, CD163, CD206, CD20, and PD-L1 positive cell densities were higher at the tumor-stroma interface than in the tumor-core (CD3: 77 vs. 50 cells/mm2, p = 0.002; CD8: 131 vs. 76 cells/mm2, p = 0.035; FOXP3: 12 vs. 6 cells/mm2, p < 0.001; T-bet: 12 vs. 6 cells/mm2, p < 0.001; CD163: 392 vs. 244 cells/mm2, p = 0.01; CD206: 190 vs. 53 cells/mm2, p < 0.001; CD20: 5 vs. 1 cells/mm2, p < 0.001; PD-L1: 85 vs. 44 cells/mm2, p = 0.02). **Figure 3A.**

When patients were stratified into clinically localized (AJCC clinical stage I – III) versus clinically metastatic disease (stage IV), T-bet density was consistently lower in patients with metastatic disease across all three zones (Tumor-core: 39 versus 9 cells/mm2, p < 0.001; Tumor-stroma interface: 73 versus 45 cells/mm2, p < 0.001; Stroma: 45 vs. 12 cells/mm2, p < 0.001). None of the other immune cell types demonstrated significant differences in cellular density between clinically localized and metastatic patients. (**Supplemental Figure 1**).

ccRCC Immune Cell Clustering: B-cells Display Uniquely High Levels of Clustering and Preference for Stroma

Immune cell clustering was quantified using a normalization of the univariate Ripley's K estimate at a search-circle radius of 75µm (nK(75)). Values greater than zero indicate cellular clustering, and less than zero indicate cellular dispersion. In the tumor-core, all immune cells displayed statistically significant univariate clustering with other cells of their same type (CD8: 11.3, p < 0.001; FOXP3: 7.1, p < 0.001; T-bet: 6.7, p < 0.001; CD20: 31.0, p < 0.001; CD68: 6.9, p < 0.001; CD163: 8.1, p < 0.001; CD206: 10.2, p < 0.001)(**Figure 3B**). Notably, univariate clustering of CD20 cells in the tumor-core was substantially higher than that of the other immune cell types (p < 0.001 for all pairwise comparisons).

At the tumor-stroma interface, a bivariate normalization of the Ripley's K metric was utilized, assessing clustering between immune cells and ccRCC tumor cells. This metric effectively tests the immune cell type's proclivity for clustering into the tumor compartment (values greater than zero), or the stromal compartment (values less than zero), at the tumor-stroma interface. FOXP3 and T-bet cells did not demonstrate significant clustering with tumor cells at this location (Interface bivariate nK(75); FOXP3: -0.3, $p = 0.33$; T-bet: 1.3 , $p = 0.25$). CD8, CD68, CD163, and CD206 cells demonstrated significant clustering into the tumor compartment (CD8: 2.0, $p = 0.02$; CD68: 8.1, $p < 0.001$; CD163: 4.5, $p < 0.001$; CD206: 7.3, $p < 0.001$). Interestingly, CD20 cells were outliers in this regard and demonstrated significant clustering into the stromal compartment (CD20: -6.25, $p < 0.001$). (**Figure 3C**).

An illustrated example depicting the overall density and clustering distributions of the included immune cell markers is available in **Figure 3D**.

Recurrent Somatic Mutations affect Immune Cell Density in the Tumor-core

Fifty-six patients in the ccRCC cohort previously underwent whole exome DNA sequencing from which we identified recurrent somatic mutations: BAP1 (4/56 patients, 7.1%) , KDM5C (9/56, 16.1%), MTOR (4/56, 7.1%), PBRM1 (22/56, 39.3%), PTEN (5/56, 8.9%), SETD2 (8/56, 14.3%), and VHL (42/56, 75.0%). Patients with MTOR alterations had significantly lower tumor-core cell density of T-bet+ T-cells (29 vs. 13 cells/mm^2; $p < 0.001$), CD163+ macrophages (264 vs. 47 cells/mm^2; $p < 0.001$), and CD206+ macrophages (65 vs. 18 cells/mm^2; $p < 0.001$) (**Figure 4A**). Patients with SETD2 alterations had significantly lower tumor-core cell density of CD8+ T-cells (97 vs. 30 cells/mm^2; $p = 0.002$), and PD-L1 positivity (70 vs. 13 cells/mm^2; $p = 0.02$)(**Figure 4B**). PBRM1 alterations were not associated with significant differences in immune cell censity (**Figure 4C**). Comparisons for other alterations can be found in **Supplemental Figure 2**.

RNA-seq Immune Cell Gene Expression is Inconsistently Associated with mIF Density

Bulk RNA-seq data was obtained from tumor-core samples in 116 patients, 92 with ccRCC. Correlation was determined between tumor-core cell density as determined by mIF, and xCell score; an RNA-seq based gene expression score quantifying relative expression of 64 different immune cell types. Relevant comparisons were made between xCell cell-types and corresponding mIF marked cell types.

Within the ccRCC cohort, CD8+ xCell score and CD8+ mIF cell density were strongly correlated (Spearman's R = 0.63). Moderate correlation was found between B-cell xCell score and CD-20+ mIF cell density (R = 0.42), T-reg xCell score and FOXP3+ mIF cell density (R = 0.38), and a generalized xCell macrophage score with CD-68+ mIF cell density (R = 0.34). Poor correlation was identified between M2 macrophage xCell score and CD163+ and CD206+ mIF cell density (R = -0.16), and Th1 T-cell xCell score and T-bet+ mIF cell density (R = -0.23). A correlation matrix for the ccRCC cohort is available in **Figure 4D**.

Low Angiogenesis and High T-effector Score Tumors are Infiltrated with CD8+ T-cells and CD68+ TAMs

Angiogenesis and T-effector gene signature scores, previously derived from the IMmotion150 trial data, were determined for 92 patients with ccRCC[12]. Patients with high angiogenesis scores had significantly lower mIF cell densities of CD68+ and CD8+ cells in the tumor-core ($p = 0.002$ and $p = 0.05$, respectively), stroma ($p = 0.04$ and $p = 0.05$, respectively), and tumor-stroma interface zones ($p < 0.001$ and $p = 0.001$, respectively) (**Figure 4E**). Patients with high T-effector scores had significantly higher tumor-core mIF cell densities of CD68+ ($p < 0.001$), CD8+ ($p = 0.002$), FOXP3+ ($p = 0.04$), and PDL1+ cells ($p = 0.02$)(**Figure 4F**).

CD163+ TAM and Tumor Cell Clustering is Significantly Associated with Survival

In the ccRCC cohort, survival outcomes were determined for each of the mIF-derived cell density and geospatial metrics using median cut-point cohort stratification and false discovery rate adjusted multivariable Cox proportional hazards models accounting for patient age and SSIGN score[28]. Outcomes included OS, cancer-specific survival (CSS), and recurrence-free survival (RFS).

An example mIF image of a slide with low tumor/CD163 nK(75) at the tumor-stroma interface is displayed in **Figure 5A**. At the tumor-stroma interface, tumor/CD163 nK(75) and CD163 cell density demonstrated poor but statistically significant correlation ($R = 0.27$, $p < 0.001$), demonstrating that these metrics are not redundant (**Figure 5B**).

Bivariate clustering between CD163+ TAMs and tumor cells at the tumor-stroma interface was strongly associated with OS and CSS. Specifically, patients with higher clustering of CD163+ TAMs into the tumor compartment at the tumor-stroma interface had better survival outcomes (Tumor/CD163+ nK(75): median OS – hi = 149mo., lo = 86mo., FDR-adj. Cox $p < 0.001$; median CSS – hi = 174mo., lo = 85mo.; FDR-adj. Cox $p < 0.001$) (**Figure 5C**). CD163+ cell density was not associated with OS or CSS (**Figure 5D**). None of the mIF density or geospatial clustering metrics were associated with RFS on the FDR-adjusted Cox proportional hazards regression (**Supplemental Table 1**).

When stratified into AJCC clinical stage, median Tumor/CD163+ nK(75) at the interface decreased in a stepwise fashion (Stage I/II: 4.4 (IQR -0.5-5.1); Stage III: 1.4 (IQR -0.3-3.5); Stage IV: 0.6 (IQR -2.1-2.1); $P = 0.04$ between Stage I/II and Stage IV), while median CD163+ cell density at the interface was similar across clinical stages (Stage I/II: 431 cells/mm^2 (IQR 178-762); Stage III: 398 cells/mm^2 (IQR 130-735); Stage IV: 289 cells/mm^2 (IQR 137-703); $P > 0.2$ for all comparisons) (**Figure 5E and 5F**).

We further examined a small subset of 27 patients in the cohort who had advanced ccRCC and received systemic targeted therapy (n = 19) or immunotherapy (n = 9), with one patient receiving combination targeted- and immunotherapy. Per RECIST response criteria, patients who responded to

therapy had higher median Tumor/CD163+ nK(75) values than those who did not respond (1.5 vs. -1.2, respectively; p = 0.10), particularly in the immunotherapy subgroup (7.7 vs. 1.7, respectively; p = 0.20), though these differences were not statistically significant (**Figure 5G**).

Tumor/CD163 Clustering Gene Expression Score

A CD163 clustering differential gene expression score was developed using bulk RNA-seq data and Tumor/CD163+ nK(75) values at the tumor-stroma interface in the ccRCC cohort. The expression score was trained and tested on independent groups within our cohort, confirming strong correlation with Tumor/CD163+ nK(75). This score was then applied to ccRCC patients identified in the TCGA KIRC cohort of ccRCC patients. Higher expression scores reflect higher Tumor/CD163+ nK(75) values, indicating clustering of CD163+ TAMs into the tumor compartment at the tumor-stroma interface. The 24 genes included in the CD163 clustering expression score are listed in **Figure 6A**.

In the TCGA cohort (n = 469), median CD163 clustering expression was significantly higher in patients with AJCC clinical stage I/II tumors versus those with stage III and stage IV (Stage I/II: 2.3 (IQR 0.2-3.6; Stage III: 0.8 (IQR -0.9-2.8); Stage IV: 1.1 (IQR -1.6-2.5)) (**Figure 6B**), similarly to the result seen for Tumor/CD163+ nK(75) in the mIF cohort (**Figure 5E**). When stratified by the median, patients with low CD163 clustering expression scores had substantially worse OS (log-rank $p < 0.01$), in a similar manner to that seen for Tumor/CD163+ nK(75) in the mIF cohort (**Figures 6C and 6D**). Likewise, patients with low CD163 clustering expression scores had substantially worse ccRCC specific survival (log-rank $p < 0.01$), in a similar manner to that seen for Tumor/CD163+ nK(75) in the mIF cohort (**Figures 6E and 6F**).

CD8+ Clustering versus Conventional CD8+ Inflamed, Desert, and Excluded Categories

Example mIF images demonstrating high and low bivariate Tumor/CD8 clustering at the tumor-stroma interface are depicted in **Figure 7A**. High bivariate clustering between CD8+ T-cells and tumor

cells at the tumor-stroma interface was strongly associated with improved OS and CSS (Tumor/CD8+ nK(75): median OS – hi = 149mo., lo = 68mo., FDR-adj. $p < 0.001$; median CSS – hi = 174mo., lo = 69mo., FDR-adj. Cox $p < 0.001$)(**Figure 7B**).

Patients with ccRCC were stratified into conventional CD8+ inflamed, desert, and excluded categories based on differential cell-density within the tumor-core and stromal histologic zones, as previously described[16]. KM estimates did not identify an association between these categorizations and OS (log-rank P = 0.13) (**Figure 7C**). Patients classified as having high stromal clustering of CD8+ cells at the tumor-stroma interface had an even distribution of classification into the inflamed, excluded, and desert categories (n = 17, 15, and 12, respectively), whereas patients classified as having CD8+ cells clustered into the tumor compartment at the tumor-stroma interface were heavily skewed toward the inflamed category (Inflamed = 31 patients, excluded = 4, desert = 9) (**Figure 7D**).

Stromal Co-localization of CD163+ TAMs and CD8+ T-cells at the Tumor-stroma Interface

Tumor/CD8+ and Tumor/CD163+ nK(75) were weakly correlated among all ccRCC patients (Spearman's R = 0.22, p = 0.05; **Figure 7E**). Patients were then stratified by concordance of geospatial clustering of CD8+ and CD163+ cells at the tumor-stroma interface. If both cell-types demonstrated clustering into the tumor compartment, they were determined to be "co-localized in the tumor", if both were clustered into the stromal compartment they were "co-localized in the stroma", and other samples were not considered to demonstrate co-localization (**Figure 7E**).

OS was substantially worse for patients with CD8+/CD163+ stromal co-localization and improved in a stepwise manner for patients with no-colocalization, followed by patients with CD8+/CD163+ tumor co-localization who had favorable OS (median OS: 64mo., 116mo., 178mo., respectively; log-rank $p < 0.001$)(**Figure 7F**). Patients with CD8+/CD163+ stromal co-localization had a higher proportion who presented with AJCC clinical stage IV (7/21 patients, 33.3%), as compared with patients with

CD8+/CD163+ tumor co-localization (4/22 patients, 18.2%) (**Figure 7G**). Of the 27 patients who received systemic targeted- or immunotherapy, 6 patients had CD8+/CD163+ stromal co-localization, and none responded to therapy (0/6 patients, 0%), as compared with 5 out of 14 responding in the no-colocalization group (35.7%), and 4 out of 7 patients responding in the CD8+/CD163+ tumor co-localization group (57.1%) (**Figure 7H**). Similarly, for the subgroup of patients who received immunotherapy 0/2 patients responded in the CD8+/CD163+ stromal co-localization group (0%), 2/4 patients responded in the no co-localization group (50%), and 2/3 patients responded in the CD8+/CD163+ tumor co-localization group (66.6%).

DISCUSSION

Leveraging mIF, digital pathologic image analysis, and empirical geospatial clustering models, we outlined a global view of immune cell spatial distribution within the RCC microenvironment and identified highly specific cellular distributions that were significantly associated with clinical outcomes. Namely, clustering of M2-like CD163+ macrophages and CD8+ T-cells into the stromal compartment at the tumor-stromal interface was associated with more advanced clinical stage and significantly worsened OS and CSS. To our knowledge, this report is the first to describe these novel spatial dynamics and their clinical associations in RCC.

M2-like macrophages are increasingly being recognized as an important a pro-tumor component of the RCC TIME[20,26,29,30]. In contrast with pro-inflammatory M1-polarized macrophages, M2-like TAMs are associated with tissue remodeling, secreting a variety of growth factors and proteases, and have consistently been implicated in conferring a pro-tumor effect on the TIME[30]. A landmark mass cytometry study of the RCC TIME by Chevrier et al in 2017 identified that a specific macrophage cluster, labeled as M-11, was associated with more advanced disease[17]. The most specific surface marker for cluster M-11 was CD163, a high affinity scavenger receptor that is a classical marker of M2-like TAMs[17,29]. Recent

scRNA-seq studies have further associated M2-like TAMs with poor clinical outcomes, and implicated these cells in switching tissue-resident CD8+ cells into a terminally exhausted state via specific receptor-ligand interactions [20-22].

Most hypothesized mechanisms for the M2-like TAM pro-tumor effect rely on close proximity to their effector cell, and as such we aimed to associate measures of geospatial TAM clustering with clinical outcomes. Previous work by our group identified worse OS in patients with increased interface clustering of tumor cells and CD68+ TAMs, a pan-macrophage marker, in a small cohort of patients with metastatic ccRCC who subsequently received IT, further supporting the notion that TAM spatial distribution can affect outcomes[25]. In the present study, we identified more advanced clinical stage and substantially worse OS and CSS for patients with CD163+ M2-like TAMs clustered into the stromal compartment at the tumor-stroma interface.

In light of recent studies highlighting immunosuppressive receptor-ligand interactions between CD8+ T-cells and M2-like TAMs, we stratified patients by co-localization of CD8+ and CD163+ immune cells at the tumor-stroma interface, and found that co-localization of these cells in the stromal compartment was associated with poor clinical outcomes, as compared to co-localization in the tumor compartment[20].

The biologic underpinnings of this association are unclear but could be driven by an environmental niche in the stromal compartment that favors receptor-ligand interactions between CD8+ T-cells and CD163+ TAMs, potentiating their immunosuppressive pro-tumor effect. This hypothesis is supported by a 2018 study by Peranzoni et al, who demonstrated that CD8+ T-cells develop impeded motility and poor tumor-migration after coming in direct contact with stromal TAMs, a high proportion of which expressed CD163[24]. CD8+ T-cell motility and tumor-migration was then restored following depletion of stromal TAMs from the specimen[24]. Additionally, studies have consistently shown that elimination of myeloid-derived suppressor cells from the ccRCC TIME results in enhancement of anti-

tumor T-cell infiltration and effect[31,32]. Our findings imply that these CD8-TAM geospatial interactions within the stroma may translate to substantial clinical impact. Further study will be necessary to elucidate the exact nature of these interactions.

A major goal of this research is to facilitate the discovery of adjunctive macrophage-targeted therapies to improve response rates to ICI therapy. Promising data is emerging for the ability of such treatments, including CCR2 antagonists, to augment anti-tumor immunity when given in combination with ICIs[33]. The success of these endeavors will hinge on biomarker discovery to identify specific cohorts of patients who will benefit from adjunctive macrophage-targeted therapy. The results of our analysis imply that characterization of M2-like TAMs in the stromal compartment at the tumor-stromal interface would likely be the highest yield for identifying macrophages that negatively impact clinical outcomes.

Another interesting finding in this analysis was that patients with high clustering of CD8+ T-cells into the stromal compartment at the tumor-stroma interface has worse OS and CSS. Infiltration of CD8+ T-cells has been associated with improved ICI response and OS in several primary solid tumors, but has been paradoxically associated with poor clinical outcomes in RCC[16]. In this study, no OS associations were identified using conventional CD8+ metrics stratifying patients into “inflamed”, “desert”, and “excluded” categories by their differential tumor-core and stroma CD8+ immune cell densities. However, significantly worse OS was seen in patients with CD8+ clustering into the stromal compartment at the tumor-stromal interface, a cellular distribution that is conceptually in-line with immune cell exclusion. Further study is needed to validate this finding in external cohorts, but it is possible that bivariate geospatial clustering metrics measured at the tumor-stromal interface result in a more accurate and biologically meaningful framework for determining immune cell exclusion.

Future directions for this research will aim to ameliorate the limitations to the present analysis, while expanding upon the most clinically pertinent cohort. In this analysis, CD8 and CD163 markers were on separate mIF marker panels. As such, a direct geospatial analysis of clustering between these cell

types was not possible, and an indirect measure was utilized to stratify into cohorts whose cells demonstrated similar distributions at matched locations. Additionally, the lymphoid panel was not designed to detect markers of CD8+ terminal exhaustion. The cohort of clinical stage IV patients was not large enough (n = 27) to adequately address the question of clinical response, particularly in the IT subgroup (n = 9). Further efforts will be devoted to a larger cohort of patients with stage IV disease, including M2-like TAM and CD8+ exhaustion markers in the same mIF panel, as to directly measure the geospatial clustering between these cells. Furthermore, spatial transcriptomic analysis would certainly build upon these marker-based findings, associating geospatial distributions with specific RNA transcripts and signatures.

METHODS

Patient and Sample Selection

We obtained 122 primary tumor samples from 122 patients with RCC, from the years 2004-2018, through protocols approved by the institutional review board (H. Lee Moffitt Cancer Center and Research Institute's Total Cancer Care protocol; Advarra IRB Pro00014441). Samples were obtained via surgical excision. Written informed consent was obtained from all tissue donors. Patients were included in this study if they provided written consent to the molecular characterization of their tissue and did not receive any systemic therapy prior to tissue collection.

Multiplex Immunofluorescence

Prior to multiplex IF, tissue blocks were prepared, and an experienced genitourinary pathologist (JD) reviewed each slide obtained from formalin-fixed paraffin-embedded tissue samples and annotated 7 spatially distinct regions of interest (ROIs) from 3 predetermined tumor zones: 2 ROIs from the tumor core, 3 from the tumor-stroma interface, and 2 from the stroma. The tumor-core ROIs studied were

selected regions with high tumor cell content, and without evidence of grossly necrotic tissue. The tumor-stroma interface ROIs were selected to contain approximately equal parts of tumor and stromal tissue.

Tissue samples were then stained using the PerkinElmer OPAL 7 Color Automation Immunohistochemistry Kit (PerkinElmer, Waltham, MA) on the BOND RX Autostainer (Leica Biosystems, Vista, CA). In brief, tissue slides were sequentially stained in 2 panels using antibodies against CD3, CD8, CD20, CD68, CD163, CD206, forkhead box P3 (FOXP3), T-box transcription factor TBX21 (T-Bet; a T-box protein expressed in T cells), epidermal growth factor receptor (EGFR), and programmed death-ligand 1 (PD-L1). These markers were selected for their previously demonstrated frequency in ccRCC[17].

All subsequent steps, including deparaffinization, antigen retrieval, and staining, were performed using the OPAL manufacturer's protocol. Pan-cytokeratin (PCK) and 4',6-diamidino-2-phenylindole (DAPI) counterstaining were applied to all slides, and imaging was performed using the Vectra3 Automated Quantitative Pathology Imaging System (PerkinElmer). Importantly, PCK was applied only after confirmation of tumor content by examination of H and E images for each ROI. Multilayer TIFF images were exported from InForm (PerkinElmer) and loaded into HALO (Indica Labs, Albuquerque, NM) for quantitative image analyses[34]. The size of the ROIs was standardized at 1356 × 1012 pixels, with a resolution of 0.5 µm/pixel, for a total surface area of 0.343 mm^2. Using HALO, for each staining marker a positivity threshold within either the nucleus or cytoplasm was set, and the entire image set was analyzed. From this analysis, generated data included the total cell count, positive cell counts for each IF marker, fluorescence intensity of every individual cell, percent of cells that were positive for each marker, and Cartesian coordinates for their location in the ROI image.

Whole Exome DNA Sequencing

These same tissue blocks were used to extract tumor DNA for sequencing, which determined

the presence of somatic mutations in ccRCC tumors. These same tissue blocks were used to extract tumor DNA for sequencing, which determined the presence of somatic mutations in ccRCC tumors. Sequence reads were aligned to the reference human genome with the Burrows-Wheeler Aligner (BWA)[35], and insertion/deletion realignment and quality score recalibration were performed with the Genome Analysis ToolKit (GATK)[36]. Tumor specific mutations were identified with Strelka[37] and MuTect[38], and were annotated to determine genic context (ie, non-synonymous, missense, splicing) using ANNOVAR[39] and summarized using in-house Perl and R scripts

Geospatial Analysis

For each ROI in our IF analysis, cell density was determined for each IF marker and for a subset of dual-positive markers. For each sample, ROI cell densities were averaged within each tumor zone (tumor core, stroma, and tumor-stroma interface) such that one density value remained for each zone in each sample. This stratification allows for broad macro-level comparisons of immune cell densities across each tumor zone.

A quantitative framework leveraging Ripley's K estimates, a methodology for quantifying spatial heterogeneity most commonly utilized in ecology and economics, was utilized to assess complex local geospatial relationships among tumor cells, stromal cells, and immune cells [40]. ROIs containing ≥10 cells positive for a relevant marker were considered eligible for spatial analysis. As there is no previously validated standard for this cutoff, the ≥10 cell cutoff was agreed upon through consensus of the authors.

The Ripley's K function (K(r)) measures the number of points within a search-circle containing a point at its center, repeating this process for each point of interest and summating/averaging the results, then repeating this process across a range of search-circle radii (r) [40,41]. The resultant distribution can then be compared to an estimated distribution of complete spatial randomness, assuming a Poisson process. Edge correction is necessary to account for points that are near the boundary of the

observation window, where a portion of the search-circle falls beyond this boundary [42,43]. Isotropic edge correction was utilized in this study, adjusting the K(r) value by the ratio of the search-circle circumference within and beyond the boundary of the observation window.

K(r) values were determined for each chosen metric within each ROI, using isotropic edge correction, and the following normalization was applied : $nK(r) = \sqrt{(K(r) / \pi)} - r$, which is sometimes described as either the "H-function" or "L(r) – r" [41,44]. This normalization is an improvement of the naïve Ripley's K function in that the expected value of nK(r), reflecting complete spatial randomness and assuming a Poisson process, is 0 across all values of r, facilitating interpretation and comparison of the results across values of r. After application of this normalization the expected variance for complete spatial randomness becomes relatively consistent across all values of r. Values of nK(r) > 0 represent cellular clustering and values < 0 represent cellular dispersion. The theoretical range of possible nK(r) values is negative infinity to positive infinity. A one-sample Wilcoxon signed-rank test can be used to compare the nK(r) value for a group of samples at any given radius to 0, the expected value of complete spatial randomness.

nK(r) can be applied in a univariate (ex: assessing clustering among cell-type A with other cell-type A cells) or bivariate (ex: clustering of cell-type A with cell-type B) manner. In the tumor-core and stromal zones, univariate clustering was utilized for each IF-marker. At the tumor-stroma interface, bivariate clustering with tumor cells was assessed for each IF-marker, to assess the affinity for the marked immune cells to exist in the tumor or stromal compartment in this zone. A radius of 75um was selected (accommodating approximately 3 ccRCC tumor cells) to reflect clustering in the vicinity of the cell of interest.

All spatial analysis was conducted using the *spatstat* package for R statistical computing software[43].

RNA-seq Immune Cell Expression and IMmotion150 Angiogenesis and T-effector scores

A subset of patients in the IF cohort (n = 116) had tumor samples that had previously undergone bulk RNA sequencing of macro-dissected tumor samples. The TruSeq RNA Exome kit (Illumina) for 50 million 100–base pair paired-end reads was utilized, and RNA sequence reads were aligned to the human reference genome in a splice-aware fashion using Spliced Transcripts Alignment to a Reference (STAR) [45], allowing for accurate alignments of sequences across introns. Aligned sequences were assigned to exons using the HTseq package[46] to generate initial counts by region. Normalization, expression modeling, and difference testing were performed using DESeq2 [47].

RNA sequencing data was analyzed for cell-type enrichment using the xCell bioinformatic pipeline[48]. xCell uses a compendium of validated gene expression signatures for 64 individual cell-types derived from thousands of expression profiles. Single-sample gene set enrichment analysis scores were adjusted for spillover compensation to generate an adjusted enrichment score for each cell type within the specimen, which is referred to as the xCell score[48]. xCell scores were generated for each of the 64 cell-types for each tumor specimen. Notably, the tumor samples utilized for RNA sequencing were almost entirely composed of tumor tissue, by volume, and therefore are expected to most closely resemble the tumor-core zone from the IF analysis. Relevant comparisons were made between xCell cell-types and corresponding mIF marked cell types.

CD163+ Interface Clustering Gene Expression Score

An exploratory analysis regarding differential gene expression was performed as it related to Tumor/CD163+ nK(75) at the tumor-stroma interface, as this was the strongest predictor of overall survival and clinical stage in our cohort and is directly relevant to the currently accepted model of immunotherapy response and resistance in ccRCC.

81 samples had overlapping RNA-seq and mIF data. The correlation between each gene and

Tumor/CD163+ nK(75) was calculated, resulting in 24 unique genes (**Figure 6A**) with an r^2 (Pearson) > 0.3, $p<0.01$, median expression >1 and a range larger than 1. This filtering ensures that the genes are expressed in most samples and that they have a range larger than 1 log2 units. These 24 genes were used as a gene signature for Tumor/CD163+ nK(75). Principal component analysis (PCA) was used to summarize and to create a model using these genes on the 81 samples in our mIF cohort. The PCA model was validated using the procedure we have earlier described in Berglund et al[49]. The first component explained 27.9% of the variation with the second component explaining 10.6%, resulting in a PC1/PC2 ratio of 2.64. Furthermore, the correlation between the PC1 loading and the Pearson correlation coefficient was $r^2=0.74$ indicating the PCA model closely describes the Tumor/CD163+ nK(75) scores. This PCA model was then applied to the TCGA ccRCC samples (n=469) to create a CD163 Clustering expression score for the ccRCC TCGA samples which was then used for further analysis.

Statistical Analysis

Cell densities and spatial metrics were abstracted as described above. Correlations were weakly negative between univariate nK(75) metrics and their corresponding marked-cell densities (-0.10 to -0.30), and correlations were consistently poor between bivariate nK(75) metrics and their corresponding marked-cell densities (-0.10 to 0.10), confirming that the nK(75) and density metrics were supplying distinct information from one another. Thus, we proceeded with treating cellular density and geospatial clustering as distinct metrics for the remainder of the analysis.

Between-groups comparisons were made using Wilcoxon signed-rank testing. Cell densities were compared across the three studied histologic zones (tumor-core, stroma, and tumor-stroma interface), and RCC histologic subtype. Both univariate and bivariate geospatial metrics were compared with the value for complete spatial randomness, zero, within marked-cell types using a one-sample Wilcoxon signed-rank test, and between marked-cell types using a two-sample Wilcoxon signed-rank

test. Cell densities were then compared across recurrent somatic mutation status, and IMmotion150 angiogenesis and T-effector gene expression scores. Spearman's correlations were made between xCell immune cell scores relevant to the markers selected for this analysis.

The survival analysis was primarily conducted using a false-discovery rate (FDR) adjusted multivariable Cox proportional hazards regressing using age and SSIGN score as covariates. Outcomes tested were OS from date of diagnosis to censoring or death at last follow up, kidney cancer specific survival from date of diagnosis to censoring or death at last follow up, and recurrence-free survival for patients who did not present with metastatic disease. Kaplan-Meier curves were utilized to visualize survival functions. A subgroup of patients with AJCC stage IV disease (n = 27) received systemic targeted therapy (n = 19) or immunotherapy (n = 9). Response to therapy was determined per RECIST 1.1 radiographic criteria[50].

Statistical significance was defined as a two-tailed $\alpha < 0.05$. All statistical analyses were conducted using R statistical software v. 4.0.2 (Vienna, Austria).

REFERENCES

1. Motzer RJ, Jonasch E, Michaelson MD, et al. NCCN Guidelines Insights: Kidney Cancer, Version 2.2020. *J Natl Compr Canc Netw.* 2019;17(11):1278-1285.
2. Motzer RJ, Tannir NM, McDermott DF, et al. Nivolumab plus Ipilimumab versus Sunitinib in Advanced Renal-Cell Carcinoma. *N Engl J Med.* 2018;378(14):1277-1290.
3. Rini BI, Plimack ER, Stus V, et al. Pembrolizumab plus Axitinib versus Sunitinib for Advanced Renal-Cell Carcinoma. *N Engl J Med.* 2019;380(12):1116-1127.
4. Motzer RJ, Penkov K, Haanen J, et al. Avelumab plus Axitinib versus Sunitinib for Advanced Renal-Cell Carcinoma. *N Engl J Med.* 2019;380(12):1103-1115.
5. Motzer R, Alekseev B, Rha SY, et al. Lenvatinib plus Pembrolizumab or Everolimus for Advanced Renal Cell Carcinoma. *N Engl J Med.* 2021.

6. Choueiri TK. 696O_PR - Nivolumab + cabozantinib vs sunitinib in first-line treatment for advanced renal cell carcinoma: First results from the randomized phase III CheckMate 9ER trial. ESMO Virtual Congress 2020; 19 Sep 2020, 2020; Virtual.
7. Pilie PG, Jonasch E. Durable complete response in renal cell carcinoma clinical trials. *Lancet.* 2019;393(10189):2362-2364.
8. Marabelle A, Fakih M, Lopez J, et al. Association of tumour mutational burden with outcomes in patients with advanced solid tumours treated with pembrolizumab: prospective biomarker analysis of the multicohort, open-label, phase 2 KEYNOTE-158 study. *Lancet Oncol.* 2020;21(10):1353-1365.
9. Farhood B, Najafi M, Mortezaee K. CD8(+) cytotoxic T lymphocytes in cancer immunotherapy: A review. *J Cell Physiol.* 2019;234(6):8509-8521.
10. Luchini C, Bibeau F, Ligtenberg MJL, et al. ESMO recommendations on microsatellite instability testing for immunotherapy in cancer, and its relationship with PD-1/PD-L1 expression and tumour mutational burden: a systematic review-based approach. *Ann Oncol.* 2019;30(8):1232-1243.
11. Miao D, Margolis CA, Gao W, et al. Genomic correlates of response to immune checkpoint therapies in clear cell renal cell carcinoma. *Science.* 2018;359(6377):801-806.
12. McDermott DF, Huseni MA, Atkins MB, et al. Clinical activity and molecular correlates of response to atezolizumab alone or in combination with bevacizumab versus sunitinib in renal cell carcinoma. *Nat Med.* 2018;24(6):749-757.
13. Senbabaoglu Y, Gejman RS, Winer AG, et al. Tumor immune microenvironment characterization in clear cell renal cell carcinoma identifies prognostic and immunotherapeutically relevant messenger RNA signatures. *Genome Biol.* 2016;17(1):231.
14. Choueiri TK, Fishman MN, Escudier B, et al. Immunomodulatory Activity of Nivolumab in Metastatic Renal Cell Carcinoma. *Clin Cancer Res.* 2016;22(22):5461-5471.
15. Carretero-Gonzalez A, Lora D, Martin Sobrino I, et al. The Value of PD-L1 Expression as Predictive Biomarker in Metastatic Renal Cell Carcinoma Patients: A Meta-Analysis of Randomized Clinical Trials. *Cancers (Basel).* 2020;12(7).
16. Braun DA, Hou Y, Bakouny Z, et al. Interplay of somatic alterations and immune infiltration modulates response to PD-1 blockade in advanced clear cell renal cell carcinoma. *Nat Med.* 2020;26(6):909-918.
17. Chevrier S, Levine JH, Zanotelli VRT, et al. An Immune Atlas of Clear Cell Renal Cell Carcinoma. *Cell.* 2017;169(4):736-749 e718.
18. Giraldo NA, Becht E, Pages F, et al. Orchestration and Prognostic Significance of Immune Checkpoints in the Microenvironment of Primary and Metastatic Renal Cell Cancer. *Clin Cancer Res.* 2015;21(13):3031-3040.
19. Vuong L, Kotecha RR, Voss MH, Hakimi AA. Tumor Microenvironment Dynamics in Clear-Cell Renal Cell Carcinoma. *Cancer Discov.* 2019;9(10):1349-1357.
20. Braun DA, Street K, Burke KP, et al. Progressive immune dysfunction with advancing disease stage in renal cell carcinoma. *Cancer Cell.* 2021;39(5):632-648 e638.
21. Bi K, He MX, Bakouny Z, et al. Tumor and immune reprogramming during immunotherapy in advanced renal cell carcinoma. *Cancer Cell.* 2021;39(5):649-661 e645.
22. Krishna C, DiNatale RG, Kuo F, et al. Single-cell sequencing links multiregional immune landscapes and tissue-resident T cells in ccRCC to tumor topology and therapy efficacy. *Cancer Cell.* 2021;39(5):662-677 e666.
23. Zhang Y, Narayanan SP, Mannan R, et al. Single-cell analyses of renal cell cancers reveal insights into tumor microenvironment, cell of origin, and therapy response. *Proc Natl Acad Sci U S A.* 2021;118(24).

24. Peranzoni E, Lemoine J, Vimeux L, et al. Macrophages impede CD8 T cells from reaching tumor cells and limit the efficacy of anti-PD-1 treatment. *Proc Natl Acad Sci U S A.* 2018;115(17):E4041-E4050.
25. Chakiryan NH, Kimmel GJ, Kim Y, et al. Spatial clustering of CD68+ tumor associated macrophages with tumor cells is associated with worse overall survival in metastatic clear cell renal cell carcinoma. *PLoS One.* 2021;16(4):e0245415.
26. Wu K, Lin K, Li X, et al. Redefining Tumor-Associated Macrophage Subpopulations and Functions in the Tumor Microenvironment. *Front Immunol.* 2020;11:1731.
27. Hajiran A, Chakiryan N, Aydin AM, et al. Reconnaissance of tumor immune microenvironment spatial heterogeneity in metastatic renal cell carcinoma and correlation with immunotherapy response. *Clin Exp Immunol.* 2021;204(1):96-106.
28. Frank I, Blute ML, Cheville JC, Lohse CM, Weaver AL, Zincke H. An outcome prediction model for patients with clear cell renal cell carcinoma treated with radical nephrectomy based on tumor stage, size, grade and necrosis: the SSIGN score. *J Urol.* 2002;168(6):2395-2400.
29. Chen T, Chen J, Zhu Y, et al. CD163, a novel therapeutic target, regulates the proliferation and stemness of glioma cells via casein kinase 2. *Oncogene.* 2019;38(8):1183-1199.
30. Kovaleva OV, Samoilova DV, Shitova MS, Gratchev A. Tumor Associated Macrophages in Kidney Cancer. *Anal Cell Pathol (Amst).* 2016;2016:9307549.
31. Najjar YG, Rayman P, Jia X, et al. Myeloid-Derived Suppressor Cell Subset Accumulation in Renal Cell Carcinoma Parenchyma Is Associated with Intratumoral Expression of IL1beta, IL8, CXCL5, and Mip-1alpha. *Clin Cancer Res.* 2017;23(9):2346-2355.
32. Sumida K, Wakita D, Narita Y, et al. Anti-IL-6 receptor mAb eliminates myeloid-derived suppressor cells and inhibits tumor growth by enhancing T-cell responses. *Eur J Immunol.* 2012;42(8):2060-2072.
33. Tu MM, Abdel-Hafiz HA, Jones RT, et al. Inhibition of the CCL2 receptor, CCR2, enhances tumor response to immune checkpoint therapy. *Commun Biol.* 2020;3(1):720.
34. Labs I. HALO, Indica Labs. Pathology Illuminated. 2021; https://indicalab.com/halo/, 2021.
35. Li H, Durbin R. Fast and accurate short read alignment with Burrows-Wheeler transform. *Bioinformatics.* 2009;25(14):1754-1760.
36. DePristo MA, Banks E, Poplin R, et al. A framework for variation discovery and genotyping using next-generation DNA sequencing data. *Nat Genet.* 2011;43(5):491-498.
37. Saunders CT, Wong WS, Swamy S, Becq J, Murray LJ, Cheetham RK. Strelka: accurate somatic small-variant calling from sequenced tumor-normal sample pairs. *Bioinformatics.* 2012;28(14):1811-1817.
38. Cibulskis K, Lawrence MS, Carter SL, et al. Sensitive detection of somatic point mutations in impure and heterogeneous cancer samples. *Nat Biotechnol.* 2013;31(3):213-219.
39. Wang K, Li M, Hakonarson H. ANNOVAR: functional annotation of genetic variants from high-throughput sequencing data. *Nucleic Acids Res.* 2010;38(16):e164.
40. Ripley BD. Modelling Spatial Patterns. *Journal of the Royal Statistical Society Series B (Methodological).* 1977;39(2):172-212.
41. Marcon E, Puech F. A typology of distance-based measures of spatial concentration. *Regional Science and Urban Economics.* 2017;62:56-67.
42. Goreaud F, Pélissier R. On explicit formulas of edge effect correction for Ripley's K-function. *Journal of Vegetation Science.* 1999;10(3):433-438.
43. Baddeley A, Turner R. spatstat: An R package for analyzing spatial point patterns. *J Stat Softw.* 2005;12(6):1-42.
44. Besag J. Contribution to the Discussion on Dr. Ripley's Paper. *Journals of the Royal Statistical Society.* 1977;B39:193-195.

45. Dobin A, Davis CA, Schlesinger F, et al. STAR: ultrafast universal RNA-seq aligner. *Bioinformatics (Oxford, England).* 2013;29(1):15-21.
46. Anders S, Pyl PT, Huber W. HTSeq--a Python framework to work with high-throughput sequencing data. *Bioinformatics (Oxford, England).* 2015;31(2):166-169.
47. Love MI, Huber W, Anders S. Moderated estimation of fold change and dispersion for RNA-seq data with DESeq2. *Genome biology.* 2014;15(12):550.
48. Aran D, Hu Z, Butte AJ. xCell: digitally portraying the tissue cellular heterogeneity landscape. *Genome Biol.* 2017;18(1):220.
49. Berglund AE, Welsh EA, Eschrich SA. Characteristics and Validation Techniques for PCA-Based Gene-Expression Signatures. *Int J Genomics.* 2017;2017:2354564.
50. Eisenhauer EA, Therasse P, Bogaerts J, et al. New response evaluation criteria in solid tumours: revised RECIST guideline (version 1.1). *Eur J Cancer.* 2009;45(2):228-247.

Acknowledgments: This study was supported by the Molecular Genomics, Tissue Core, and Biostatistics and Bioinformatics Shared Resources at the H. Lee Moffitt Cancer Center and Research Institute, an NCI designated Comprehensive Cancer Center (P30-CA076292).

Data Availability Statement: The data that support the findings of this study are available from the corresponding author upon reasonable request.

Conflict of Interest Disclosure: The corresponding author certifies that all conflicts of interest, including specific financial interests and relationships and affiliations relevant to the subject matter or materials discussed in the manuscript (ie. employment/affiliation, grants or funding, consultancies, honoraria, stock ownership or options, expert testimony, royalties, or patents filed, received, or pending), are the following: **NHC, YK, AB, AC, GJK, AH, JN, CM, DS, EK, NL, PR, MF, DJ, LW, DD, JKT, JD, AAH, and PMA** have no disclosures; **BJM** is an NCCN Kidney Cancer Panel Member and an advisor for Merck, Inc.; **PES** is an NCCN Bladder and Penile Cancer Panel Member and Vice-Chair; **JM** is an Associate Center Director at Moffitt Cancer Center, has ownership interest in Fulgent Genetics, Inc., Aleta Biotherapeutics, Inc., Cold Genesys, Inc., Myst Pharma, Inc., and Tailored Therapeutics, Inc., and is a consultant/advisory board member for ONCoPEP, Inc., Cold Genesys, Inc., Morphogenesis, Inc., Mersana Therapeutics, Inc.,

GammaDelta Therapeutics, Ltd., Myst Pharma, Inc., Tailored Therapeutics, Inc., Verseau Therapeutics, Inc., Iovance Biotherapeutics, Inc., Vault Pharma, Inc., Noble Life Sciences Partners, Fulgent Genetics, Inc., UbiVac, LLC, Vycellix, Inc., and Aleta Biotherapeutics, Inc. **JC** is a consultant for Pfizer, Inc. and Exelixis, Inc.

Funding: The described analysis was directly funded by a Department of Defense United States Army Medical Research Acquisition Activity grant (KC180139).

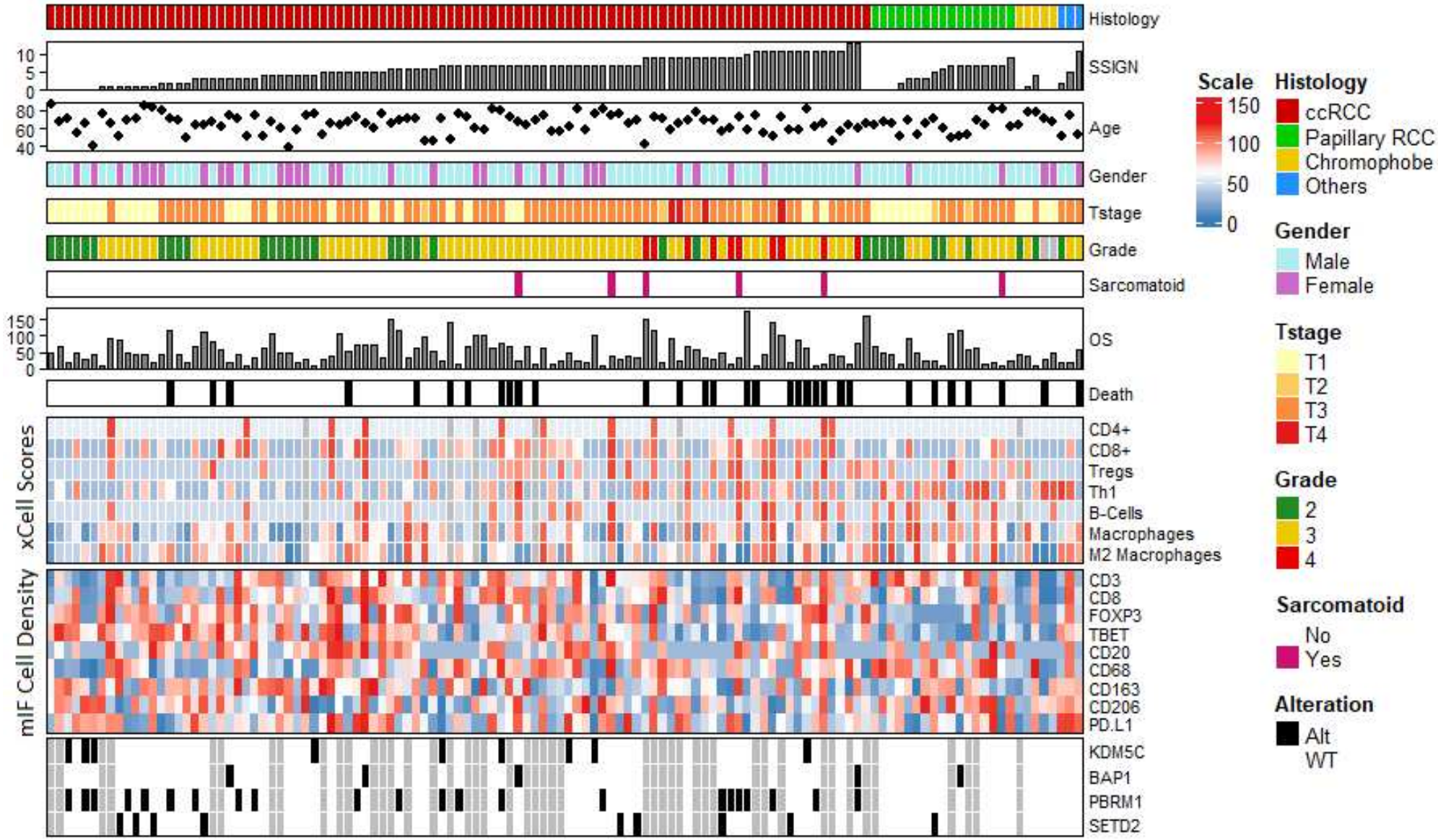

Figure 1: Overview of the demographics and selected findings from the overall cohort. Listed in descending order: RCC histologic subtype, SSIGN risk score, age, gender, pT stage, ISUP histologic grade, sarcomatoid variant status, overall survival (months), vitality status, xCell bulk RNA-seq immune expression scores, multiplex immunofluorescence cellular density in the tumor-core, and somatic mutation alteration status.

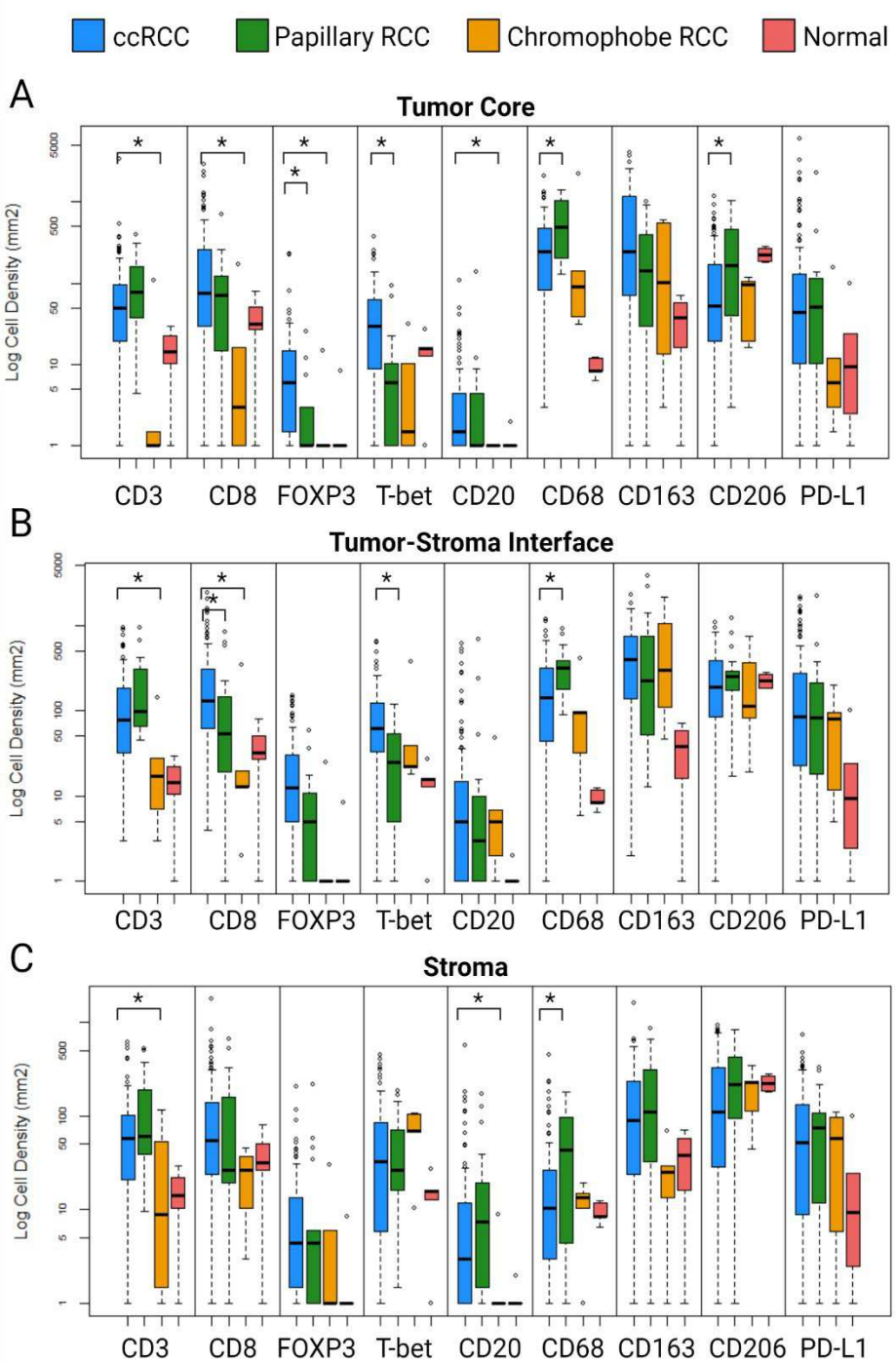

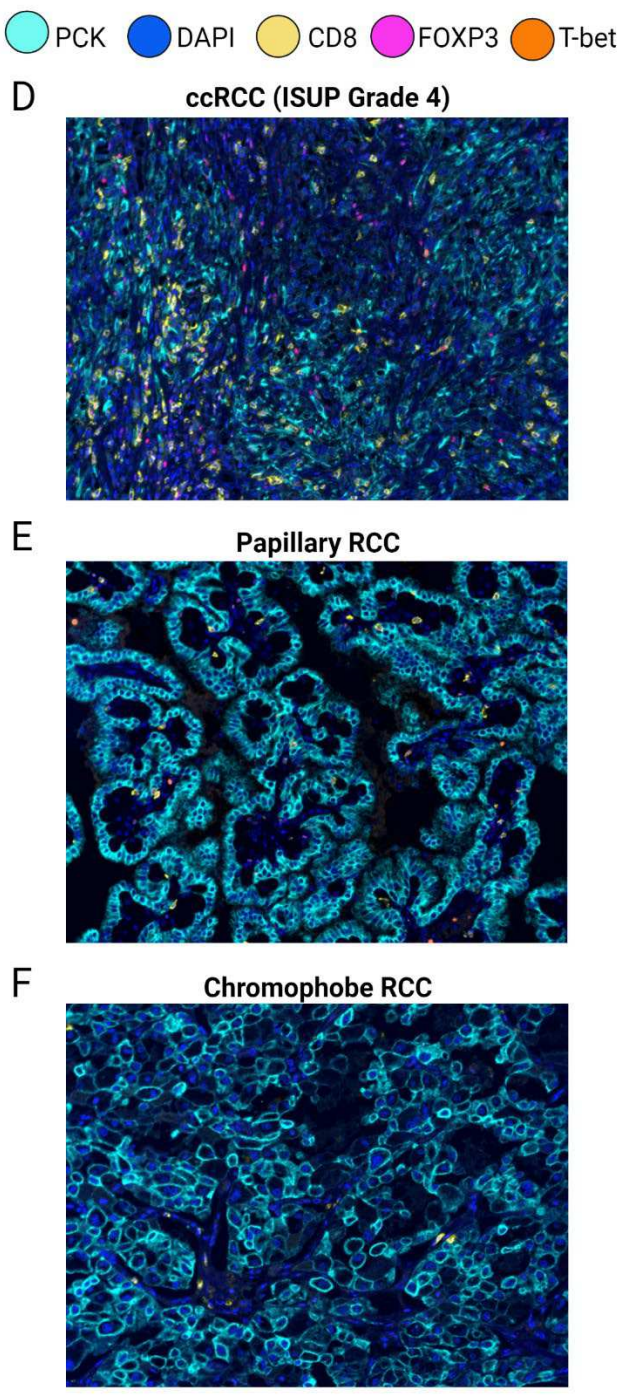

Figure 2: A-C: Differential cell densities as stratified by RCC histologic subtype (clear cell RCC, papillary RCC, chromophobe RCC, and normal kidney, across three histologic zones - A: tumor-core zone; B: tumor-stroma interface zone; C: stroma zone. D-F: Example multiplex immunofluorescence images from the lymphoid marker panel, across the RCC histologic subtypes – D: clear cell RCC; E: papillary RCC; F: Chromophobe RCC.

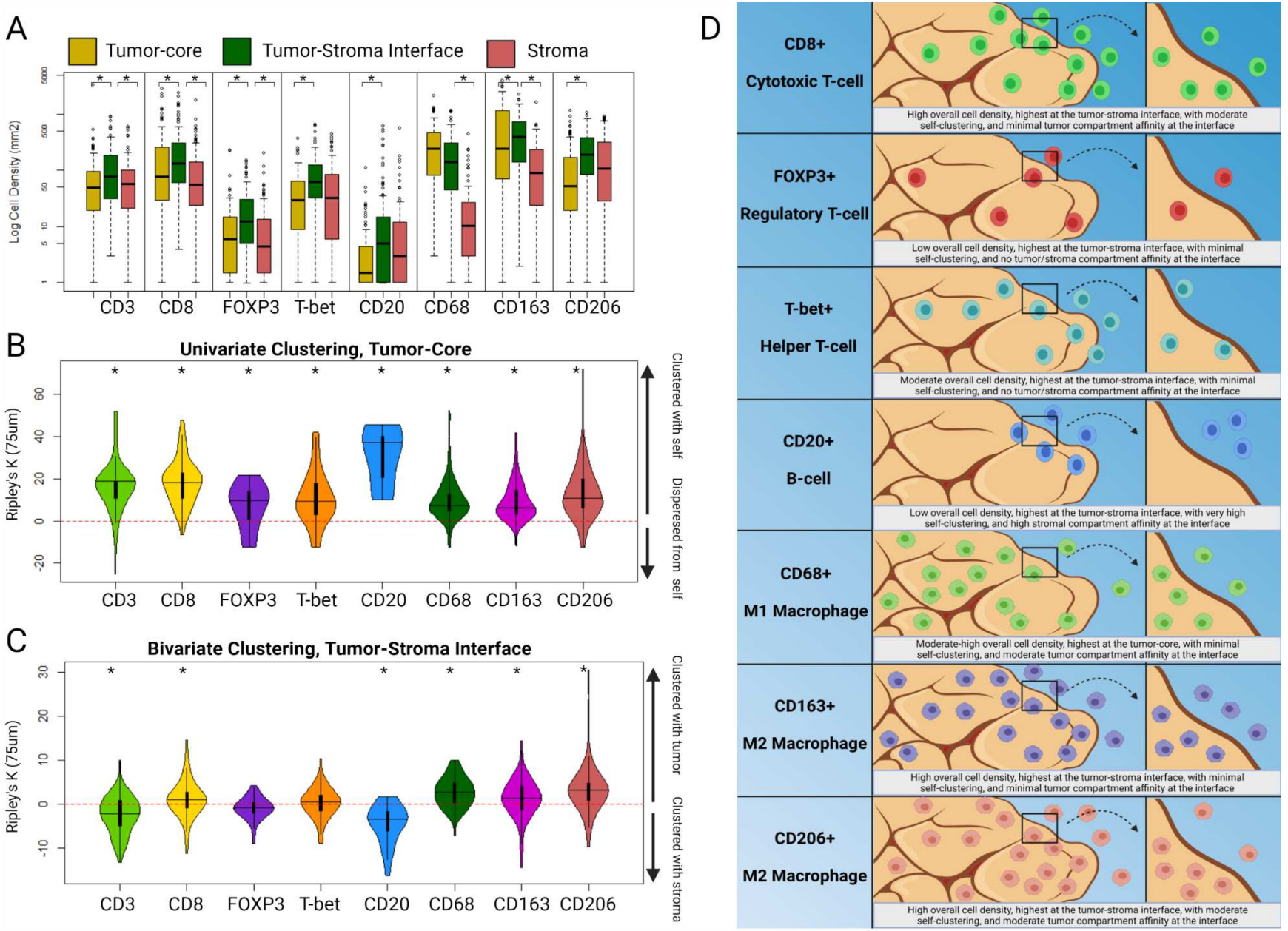

Figure 3: A: Differential cell densities stratified by histologic zone. B: Differential univariate cellular clustering, nK(75), in the tumor-core histologic zone. C: Differential bivariate clustering of tumor and immune cells, nK(75), in the tumor-stoma interface histologic zone. D: An illustrated example depicting the overall density and clustering distributions of the included immune cell markers.

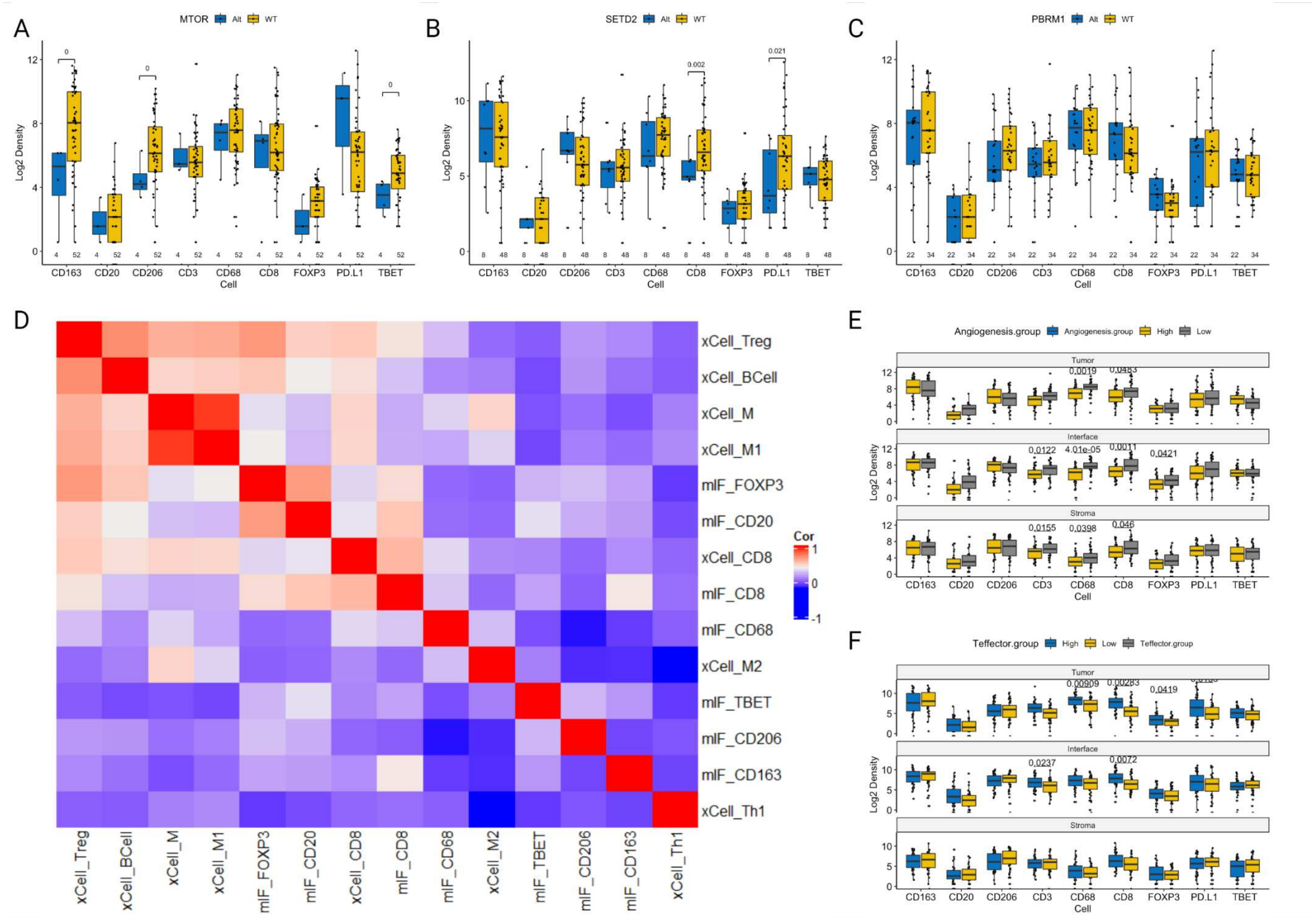

Figure 4: A-C: Differential cell densities in the tumor-core histologic zone, stratified by somatic mutation status for – A: MTOR; B: SETD2; C: PBRM1. D: Correlation matrix (Spearman) comparing xCell immune cell gene expression with multiplex immunofluorescence cell density in the tumor-core histologic zone. E-F: Differential cell densities in the tumor-core histologic zone, stratified by IMmotion150 gene signatures – E: Angiogenesis score; F: T-effector score.

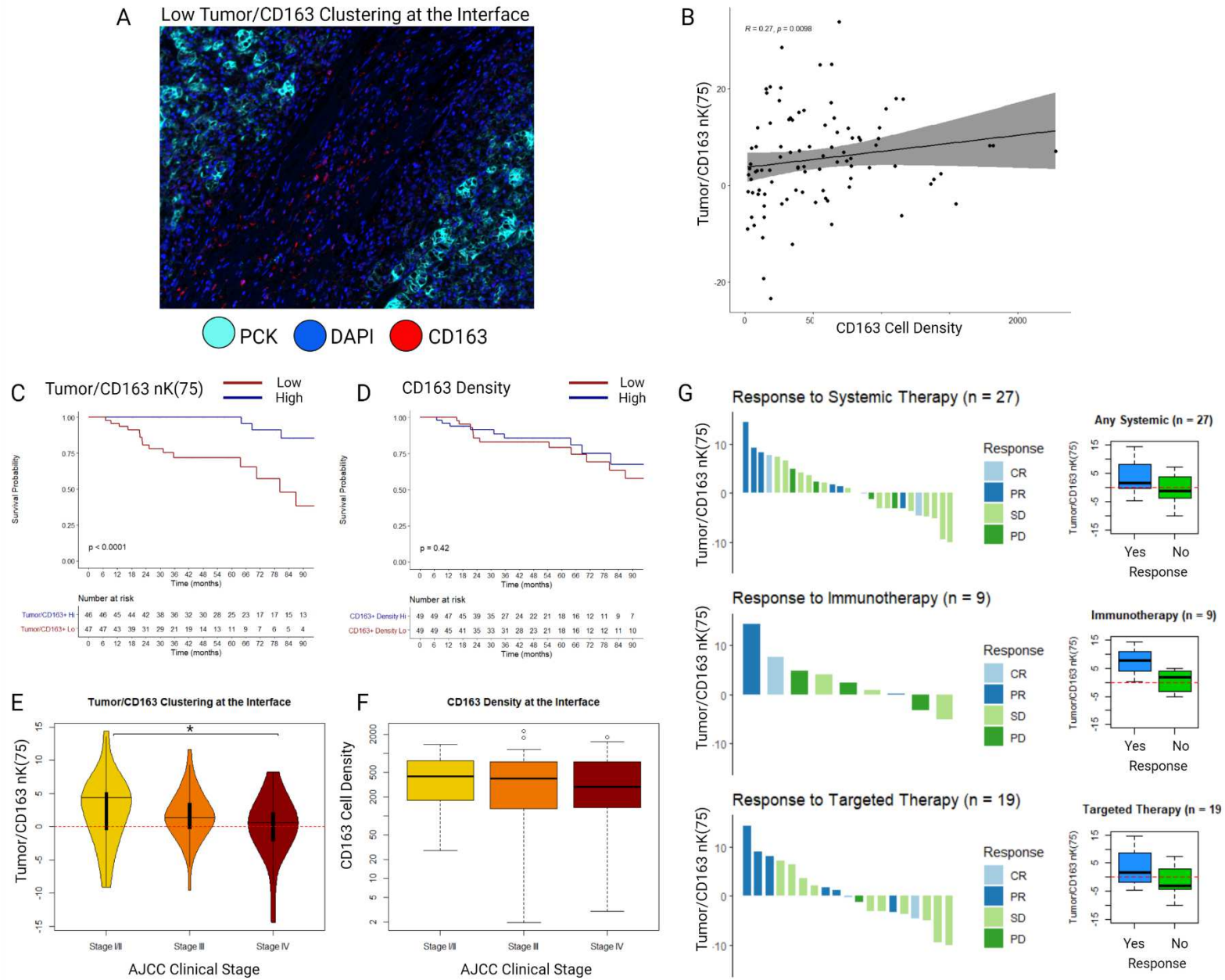

Figure 5: A: Example multiplex immunofluorescence image of a sample with low tumor/CD163 nK(75). B: Scatter plot and Spearman's correlation between CD163+ cell density and tumor/CD163 nK(75) in the tumor-stroma interface histologic zone. C: Kaplan-Meier distributions for overall survival as stratified by the median value of tumor/CD163 nK(75) in the tumor-stroma interface histologic zone. D: Kaplan-Meier distributions for overall survival as stratified by the median value of CD163+ cell density in the tumor-stroma interface histologic zone. E: Tumor/CD163 nK(75) values stratified by AJCC clinical stage at diagnosis. F. CD163+ cell density values stratified by AJCC clinical stage at diagnosis. G: RECIST responses to systemic therapy for a subgroup of patients (n = 27), either presenting with or developing clinical stage IV ccRCC, who received either systemic immunotherapy or targeted therapy. Adjacent box-plots demonstrate differences in tumor/CD163 nK(75) stratified by therapy response status.

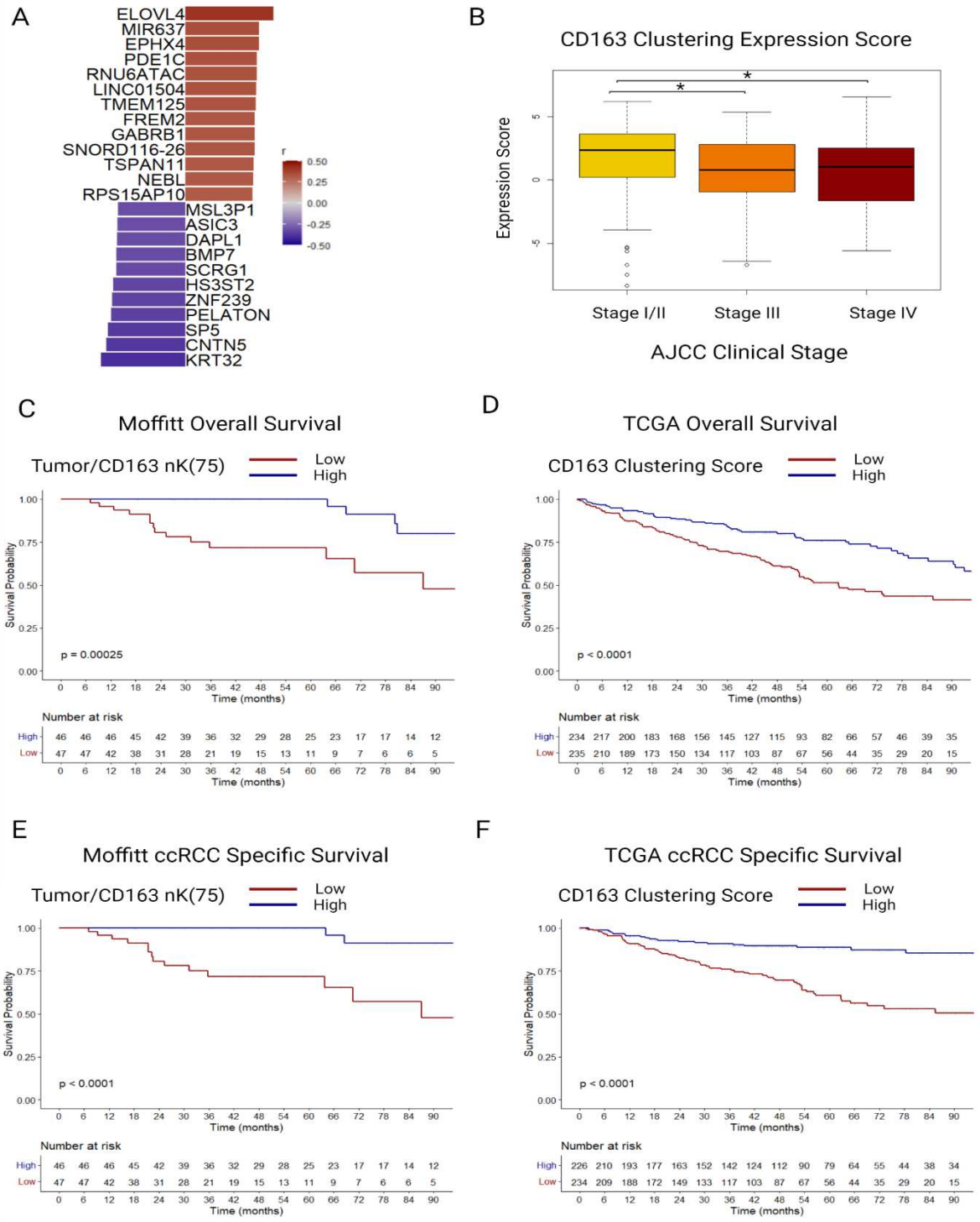

Figure 6: A: Twenty-four genes included the CD163 clustering gene expression score, ordered by Pearson correlations with Tumor/CD163 nK(75) values, all P > 0.001. B: TCGA KIRC cohort (N = 469), boxplots depicting gene CD163 clustering gene expression score by AJCC clinical stage. C: Overall survival in the Moffitt mIF cohort, stratified by the median value of Tumor/CD163 nK(75). D: Overall survival in the TCGA KIRC cohort, stratified by the median value of CD163 clustering gene expression score. E: ccRCC specific survival in the Moffitt mIF cohort, stratified by the median value of Tumor/CD163 nK(75). F: ccRCC specific survival in the TCGA KIRC cohort, stratified by the median value of CD163 clustering gene expression score.

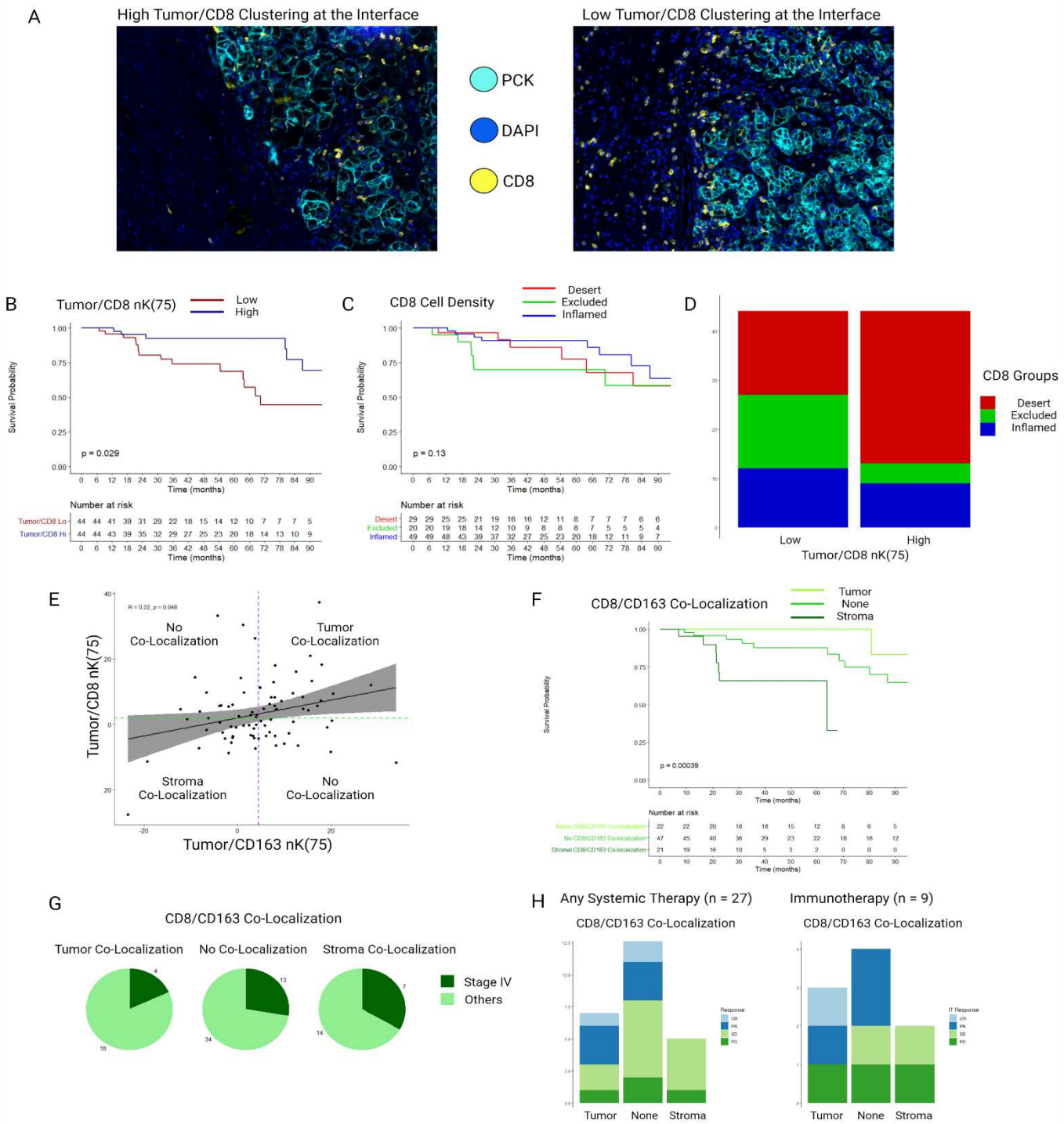

Figure 7: A: Example multiplex immunofluorescence images of a samples with high and low tumor/CD8 nK(75). B: Kaplan-Meier distributions for overall survival as stratified by the median value of tumor/CD8 nK(75) in the tumor-stroma interface histologic zone. C: Kaplan-Meier distributions for overall survival as stratified by the median value of CD8+ cell density derived infiltration, exclusion, and desert status. D: Stacked bar chart depicting proportions of patients falling in CD8+ cell density derived infiltration, exclusion, and desert groups, stratified by low and high tumor/CD8 nK(75) values. E: Scatter plot and Spearman's correlation comparing tumor/CD8 nK(75) and tumor/CD163 nK(75), overlaid with groupings by CD8-CD163 co-localization status. Purple dotted line is the median value for tumor/CD163 nK(75), green dotted line is the median value for tumor/CD8 nK(75). F: Kaplan-Meier distributions for overall survival, as stratified by CD8-CD163 co-localizations status. G: Proportion of patients diagnosed with AJCC clinical stage IV ccRCC, stratified by CD8-CD163 co-localization status. H: RECIST responses to systemic therapy for a subgroup of patients (n = 27), either presenting with or developing clinical stage IV ccRCC, who received either systemic immunotherapy or targeted therapy.

Supplementary Files

This is a list of supplementary files associated with this preprint. Click to download.

- GraphicalAbstractSupplementalFigure.pdf
- KeyResources.pdf
- SupplementalFiguresSupFig1SupFig2.pdf
- SupplementalTable1.pdf